Reliable Ocean Sensing Networks for Long-Term Deployment Using Underwater Backscatter

by

Rohan Menon

S.B., University of Washington (2023)

Submitted to the Department of Electrical Engineering and Computer Science
in partial fulfillment of the requirements for the degree of

MASTER OF SCIENCE

at the

MASSACHUSETTS INSTITUTE OF TECHNOLOGY

May 2026

© 2026 Rohan Menon. All rights reserved.

The author hereby grants to MIT a nonexclusive, worldwide, irrevocable, royalty-free license to exercise any and all rights under copyright, including to reproduce, preserve, distribute and publicly display copies of the thesis, or release the thesis under an open-access license.

Authored by: Rohan Menon
Department of Electrical Engineering and Computer Science
May 15, 2026

Certified by: Fadel Adib
Associate Professor of Media Arts and Science and Electrical Engineering and Computer Science
Thesis Supervisor

Accepted by: Leslie A. Kolodziejski
Professor of Electrical Engineering and Computer Science
Chair, Department Committee on Graduate Students

Reliable Ocean Sensing Networks for Long-Term Deployment Using Underwater Backscatter

by

Rohan Menon

Submitted to the Department of Electrical Engineering and Computer Science
on May 15, 2026 in partial fulfillment of the requirements for the degree of

MASTER OF SCIENCE

ABSTRACT

Long-term underwater sensing is essential for understanding complex ocean dynamics, yet existing systems are either tethered to costly cabled infrastructure or limited in lifetime by power-hungry modems that transmit wireless data. In this work, we report an ultra-low-power wireless underwater sensor that enables a new class of persistent ocean observation. At the core of our design is a tightly coupled sensing and connectivity architecture that leverages a recent communication technology known as underwater backscatter for energy-efficient and scalable underwater monitoring. We further extend this design to a network of sensors by introducing an SNR-aware adaptive querying technique that ensures timely and accurate measurements in the face of an unpredictable and error-prone wireless link. Deployed off the coast of Woods Hole, Massachusetts, two sensors collected conductivity, temperature, depth, and water flow data over the course of one month. Our evaluation demonstrates that this design achieves a sleep-state power consumption of only 42 μW and an estimated lifetime of approximately 2 years. Importantly, our design brings underwater backscatter from simple prototypes to reliable deployments that collect real underwater data, unlocking new possibilities across long-term climate monitoring, marine ecosystem management, and scientific discovery.

Thesis supervisor: Fadel Adib
Title: Associate Professor of Media Arts and Science and Electrical Engineering and Computer Science

Acknowledgments

First and foremost, I would like to thank my advisor, Fadel Adib. His guidance in this project and others has been invaluable in helping me grow as a researcher. I would also like to thank all of my labmates at Signal Kinetics. I feel honored to spend every day working alongside such a talented and passionate group of people. My collaborator on this project, Jack Rademacher, deserves special thanks – I have had a great time learning from him and working with him over the past two years.

I am grateful to my girlfriend, Anika, who has supported me throughout this endeavor. The other members of my household, my cats Lucy and Blue, also deserve some thanks. Finally I want to thank my family – my mom, my dad, and my brother. Every day, I realize more and more how much they have each shaped me, and how proud I am of their influence.

Contents

List of Figures 7

List of Tables 10

1 Introduction **11**

2 Results **14**

3 Approach **17**

3.1 Energy efficient sensing and computing 17

3.1.1 CTD Sensing 18

3.1.2 Current Flow Sensing 19

3.2 Asynchronous data extraction 20

3.2.1 Data and time synchronization 22

3.3 SNR-aware adaptive backscatter networking 23

4 Conclusion **26**

5 Methods **27**

5.1 Tag Implementation 27

5.2 Base Station Implementation 28

5.3 Deployment 28

5.4 Packet Structures 28

5.5 Water Flow Sensing 29

5.6 Disruption-tolerant querying 31

5.7 Lifetime Analysis 31

References 35

List of Figures

1.1 **System overview.** (a) A photograph of our tag in the ocean taken by the Woods Hole divers. On the right is a clearer view of the tag itself, illustrating its construction. (b) A photograph of the base station taken by the Woods Hole divers. (c) Deployment layout in Woods Hole, Massachusetts, showing the spatial distribution of tags and the base station. (d) Schematic of the networked architecture. First, the field of sensors (left) each senses their environment. Second, the anchored base station (right) sends acoustic downlink requests for sensor data. Third, the sensors (left) wake up and backscatter their data. Finally, the base station decodes and publishes this data (right). 11

2.1 **Collected data from Woods Hole Oceanographic Institution.** (a) From Tag 1, the four primary sensors, specific conductance in mS/cm (raw data in solid blue and median filtered in dashed blue), temperature in degrees Celsius (orange), depth in meters (purple), and current velocity in m/s (green) are plotted across calendar date spanning from April 9th to May 9th. The current flow measurements are plotted as vectors, where the length of the vector indicates the current flow velocity and its angle indicates the direction of the flow relative to geomagnetic north. The compass is illustrated in the left of the bottom panel. (b) A zoomed-in view of the last 36 hours of collected data, with the same series as shown in (a). (c) Five selected snapshots of current flow from May 1 at 6:20 AM to 9 AM for two tags, Tag 1 in blue, and Tag 2 in orange. Current flow vectors are shown as in (a), superimposed on a map showing each tag's approximate location. Below each snapshot, a trace of the depth in meters recorded by Tag 1 is shown, with a dot indicating the snapshot time. (d) A selected 72 hour segment of depth measurements from Tag 1 in blue, and Tag 2 in orange spanning from April 29th to May 2nd plotted on the left axis. The mean lower-low water level (in meters) measured by a nearby NOAA Tides and Currents Station [22] is plotted on the right axis, relative to Mean Water Low-Level. (e) Monthly temperature distributions from Aug 2025 to Jan 2026 collected from a preliminary tag deployed in the Charles River. Medians are indicated by the horizontal line, with boxes showing the 25th-75th percentile range, and whiskers indicating the full range. 15

3.1 **Developed hardware and sensor characterizations.** (a) Exploded view of the assembly of our design. (b) Motherboard PCB. (c) Daughterboard PCB. (d) Conductivity module PCB. (e) Encapsulated conductivity module. (f) Current flow sensing principle. Current flow deflects the tag at some angle θ, which is measured by an accelerometer. (g) Experimental relationship between tag tilt vs. ground truth current velocity. Points represent trial medians, with error bars indicating the 75th and 25th percentiles. The curve (dotted) shows the derived analytical model fit to the observed data. (h) Median current velocity prediction error of new experimental data vs. ground truth velocity. Error bars indicate the 75th and 25th percentiles. (i) Median percent absolute conductivity error (%) vs. ground truth conductivity (mS/cm). Error bars indicate the 75th and 25th percentiles. (j) Instantaneous power consumption (mW) of the tag's sensing cycle plotted vs. time (seconds). In sleep, the tag consumes only 42 μW of power. 17

3.2 **Asynchronous wireless sensing.** (a) Phases of the interactions between the base station (top) and the tag (bottom) plotted across time. At the bottom left in green, tag ID=1 wakes up and collects measurements into a report with sequence number 9, then goes back to sleep. Then, the base station requests sequence number 9 from tag ID=1 by transmitting a downlink command. Tag ID=1 wakes up, inserts report 9's age of 5 minutes in the response, and attempts to uplink this data to the base station. The base station fails to decode this response because of a link failure. The next request for report 9 from tag ID=1 succeeds (after a downlink request to a different tag), and the base station uses the new age (20 minutes) in the response to calculate when report 9 was actually taken (13:00). This process repeats until the base station is fully up to date with the tag's reports. (b) Block diagram of the dual-stage wakeup mechanism. Four transducers are connected in two pairs. The downlink command's envelope is detected by the carrier detector, which wakes the microcontroller from its sleep state. Then, the microcontroller enables the two amplifiers whose outputs feed into the ADC of the microcontroller, which are used to sample and decode the downlink. Finally, data previously collected from the sensors is transmitted by modulating the polarity of each pair's connection. (c) Instantaneous power consumption (mW) plotted vs. time (seconds) for a successful downlink wakeup and uplink (backscatter) cycle. (d) Instantaneous power consumption (mW) plotted vs. time (seconds) for a false downlink wakeup, where the tag successfully decodes a downlink command that was intended for a different tag ID. In this case, the tag simply ignores the command and goes back to sleep. 20

3.3 **Network metrics for a single sensor.** (a) Correlation signal-to-noise ratios (dB) vs. calendar date. The data is filtered with a moving median filter of window size equal to 5 minutes, which is the same window used in our adaptive querying technique. The blue dotted line indicates the -10 dB threshold for backing off or accelerating the rate of queries. In the following subfigures, the gray rectangles indicate the forced inactive time of the base station during which the Woods Hole divers are in the water. (b) Mean decode success rate (%) vs. calendar date. The data is filtered with a moving average filter of window size equal to 1 hour. (c) Report age (hours) vs. calendar date. (d) Polling interval (minutes) vs. calendar date. (e) CDF of the report ages in hours. (f) CDF of the number of query attempts per hour. 23

5.1 **Tilt-velocity characterization and evaluation.** (a) The flow-velocity experimental setup is pictured. The tag is dragged through the water by its bottom shackle at a number of fixed velocities by a motorized cart. A motorized pulley moves the cart, boom and tag through the water, causing the tag to experience an identical force to water flowing around the tag. (b) The tag is moved through the water at various fixed speeds inducing a tilt angle on the tag. 31

List of Tables

5.1 **Current and charge consumption analysis.** Current consumption for each stage (I_s), and the corresponding stage duration (t_s), entry count (n_s), and total stage charge (Q_s) for tags 1 and 2 under the SNR-aware adaptive querying strategy. On the right, the same information is listed under the baseline querying strategy. At the bottom are the total charge, total average current, and estimated lifetime for both querying strategies. All metrics are per 15 minute sensing interval. 33

Chapter 1

Introduction

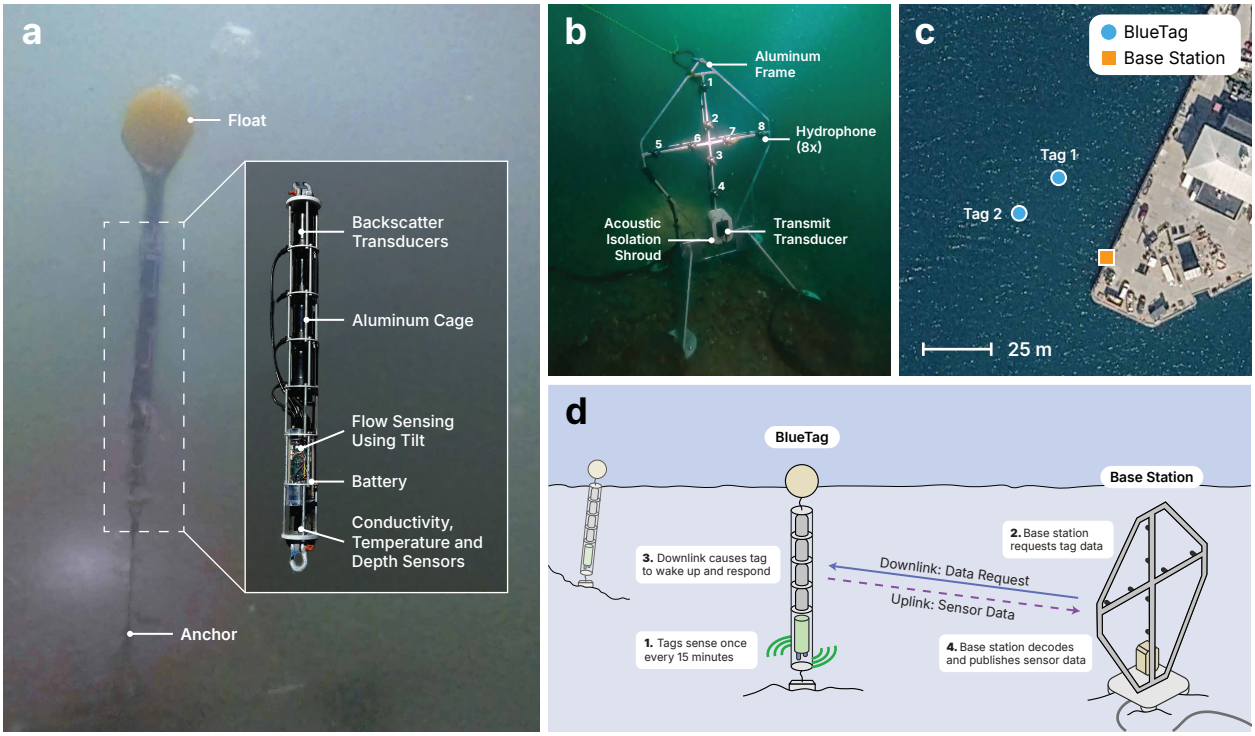

Figure 1.1: **System overview.** (a) A photograph of our tag in the ocean taken by the Woods Hole divers. On the right is a clearer view of the tag itself, illustrating its construction. (b) A photograph of the base station taken by the Woods Hole divers. (c) Deployment layout in Woods Hole, Massachusetts, showing the spatial distribution of tags and the base station. (d) Schematic of the networked architecture. First, the field of sensors (left) each senses their environment. Second, the anchored base station (right) sends acoustic downlink requests for sensor data. Third, the sensors (left) wake up and backscatter their data. Finally, the base station decodes and publishes this data (right).

Underwater sensing is a critical tool for scientific understanding of a wide variety of environmental processes, such as the carbon cycle, natural disasters, and climate change [1,2].

Monitoring these processes is important due to the ocean's central role in global economic and societal needs, including ports and shipping [3], food production [4], and coastal disaster resilience [5]. Motivated by these needs, there has been growing interest in distributed underwater sensor networks [6–8] that can enable data collection at superior spatiotemporal scale and resolution compared to localized, short-term measurements. For example, such networks could capture ecosystem data across endangered coral reefs, measure seismic activity along subsea fault lines, or monitor underwater infrastructure such as cables and pipelines.

Unfortunately, existing approaches for collecting underwater data are fundamentally limited in either the temporal or spatial scale across which they can operate. These approaches fall into two categories. The first is cabled or tethered systems that transmit data to shore or the surface through an electrical or optical link. While such systems maintain the benefit of on-demand data access and grid power, they suffer from complex deployment logistics and expensive supporting infrastructure (i.e., cables) that prevent their widespread adoption. The second is wireless platforms that use acoustic signals to communicate underwater or radio waves to communicate to shore from the surface. These platforms are limited in lifespan by the power consumption of the wireless link: existing acoustic and radio modems often consume watts of power [9–11], limiting their battery life to a few months to a year. Ideally, we need an approach that enables long-term, high-spatiotemporal resolution sensing without the infrastructure costs of cabled systems or the lifetime constraints of conventional wireless systems.

To address these challenges, we leverage an emerging wireless communication technology known as underwater backscatter [9,12]. Underwater backscatter communicates by reflecting incident acoustic waves, enabling operation at orders of magnitude lower power than traditional approaches [13,14]. Past work has demonstrated a variety of applications of underwater backscatter, including battery-free imaging, localization, and long-range and mobility-resilient communications [15–18]. However, existing work on underwater backscatter has been limited to simple prototype deployments that cannot achieve truly persistent and distributed underwater sensing. Moreover, past work has not demonstrated end-to-end networking with more than one backscatter device in the water, limiting prior efforts to temporary single-device deployments that cannot capture data over space and time.

Bringing underwater backscatter from short-term prototypes to deployable, long-term underwater networks requires a sensor design that addresses three tightly coupled problems. The first is energy efficiency: the sensor should consume as little power as possible while retaining the ability to sense its environment accurately. Additionally, the sensor's measurements should be wirelessly accessible from a remote base station. The second is scalability: the sensor should be deployable as a wireless network to enable wide-area sensing. In other words, the base station should be able to coordinate with and aggregate data from multiple sensors distributed in space. The third is data reliability: the sensor should enable regular (i.e., constant time intervals) sampling of its environment and the base station should know precisely when those samples were captured in order to support high quality ocean science.

The primary challenge with achieving these three goals simultaneously is that the underwater acoustic backscatter channel is limited in capacity and time-varying [19–21]. It is possible for any given query to a sensor to fail, which means that we cannot ask a sensor to sample its environment and return the measurement. This strategy would lead to irregularly sampled data if such a query fails. Moreover, if the acoustic channel is particularly poor

for an extended period of time, this strategy would lead to missing data that could have captured an important scientific event, such as the change in the tide. Alternatively, we could request measurements as fast as possible such that irregularly or sub-sampled data may still capture important events, but this would increase the sensor's power consumption and degrade its lifetime. Furthermore, this strategy is limited in scalability, as a network of sensors coexisting in an acoustic channel with limited capacity must now have such continuous requests distributed across the network.

Here we report an energy-efficient, scalable, and reliable underwater backscatter sensor for networked and persistent ocean sensing. Our design is based on three core capabilities that jointly enable long-term spatiotemporal monitoring. First, it introduces an energy-efficient backscatter sensor design that captures conductivity, temperature, depth, and current flow measurements every 15 minutes. This design tightly couples ultra-low-power sensing with a dual-stage wakeup trigger to keep the sensor in a microwatt-level sleep state while maintaining responsiveness to its surrounding environment and base station requests. Second, it introduces an asynchronous data extraction technique that retrieves both sensor measurements and their precise timestamps. This enables the synthesis of a regularly-sampled and time-synchronized data map even if the acoustic link fails. Finally, our design introduces an *SNR-aware* adaptive querying strategy that opportunistically retrieves data from a network of sensors when the link is strong and throttles its requests when the link is poor. This approach allows us to be responsive to the heavily time-varying underwater acoustic channel while maintaining a low power burden to the sensor network as a whole. By tightly coupling ultra-low-power sensing with wireless connectivity, this work demonstrates a new class of ocean observation systems, enabling a wide variety of persistent monitoring capabilities across climate and marine science.

We implemented an end-to-end prototype of our tag, called BlueTag (Fig. 1.1a) and deployed it in a real-world ocean environment. We deployed a network of two tags capable of measuring conductivity, temperature, depth, and current flow direction and magnitude, and distributed them over a roughly 50 by 50 meter area off the coast of Woods Hole, Massachusetts, where they collected data from April 7th to May 9th, 2026. We also implemented an end-to-end prototype of a base station that acoustically communicates with each BlueTag (shown in Fig. 1.1b) and anchored it to the seafloor. A map of our deployment is illustrated in Fig. 1.1c. As illustrated in Fig. 1.1d, tags collect data every 15 minutes which is offloaded to the base station through underwater backscatter. Prior to the networked ocean deployment, preliminary tag and reader versions were deployed in the Charles River for six months, where they collected data between Aug 2025 and Jan 2026.

Chapter 2

Results

The month-long ocean deployment captured continuous data across the four sensing modalities. Fig. 2.1a shows specific conductance, temperature, depth, and current speed from Tag 1 from April 9th to May 9th, while Fig. 2.1b highlights the final 36 hours at higher temporal resolution.

Over the course of the month, the specific conductance measurements increased slowly from approximately 42 mS/cm to 45 mS/cm. These values are consistent with the expected salinity of the coastal waters at Woods Hole. Transient dips in conductance appear in the raw data, which are likely due to small bubbles or debris depositing on the surface of the conductance cell, which is consistent with past research [23]. These dips are suppressed with a 15-point median filter, while preserving the longer-term trend.

Over the window, a gradual warming trend of roughly 5–6°C is also visible, consistent with seasonal warming during early spring. Additionally, as shown in Fig. 2.1b, the temperature data exhibits clear daily variations, with temperature increasing during daylight hours and decreasing overnight.

The depth measurements show a periodic oscillation that corresponds to the tidal cycle at Woods Hole, with two high tides and two low tides per day. Interestingly, we observed that the peak-to-peak amplitude in these depth measurements peaked near April 19th, on which the lunar phase was a new moon, generating a spring tide as expected [24].

The current flow measurements show variability that correlates with the tidal cycle observed in the depth measurements. Interestingly, high velocities correlate with periods of rising depth (flood tide) more strongly than with periods of falling depth (ebb tide). The observed pattern suggests a stronger south-eastern current during flood tide, and a weaker current when the tide is ebbing. Fig. 2.1c shows this tidal variation in current velocity across five snapshots measured by both Tag 1 (blue) and 2 (orange) from May 1 at 6:20 AM to 9 AM. Below each snapshot, the depth is plotted, with a marker indicating the snapshot time. As time progresses and the tide rises, currents measured by both tags go from being relatively weak and northeast flowing, to showing strong, southeastward flows, with a maximum velocity of 0.32 m/s, measured by Tag 1. At 9:00 AM, the tide reaches its peak and stops rising, and the tags return to measuring weak currents.

Fig. 2.1d plots the recorded depth measured by Tag 1 (blue) and 2 (orange) over a 72 hour span starting on April 29th. Both traces show the expected tidal pattern, with alternating high and low water approximately every 6 hours. As expected given the tags' proximity, their

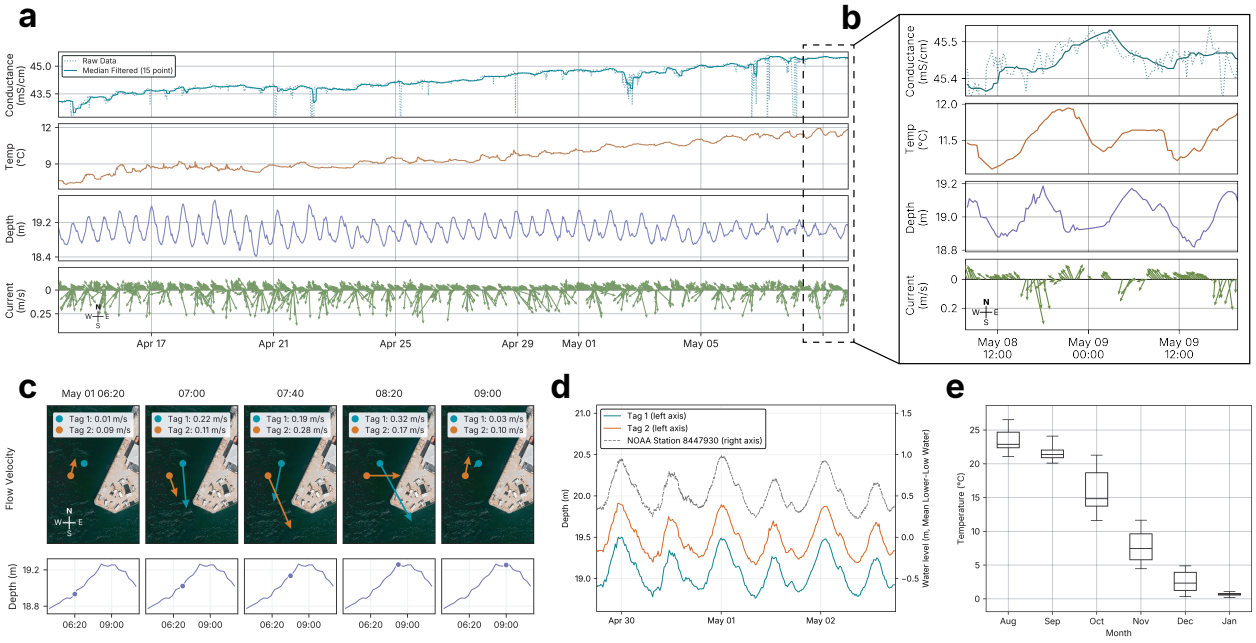

Figure 2.1: **Collected data from Woods Hole Oceanographic Institution.** (a) From Tag 1, the four primary sensors, specific conductance in mS/cm (raw data in solid blue and median filtered in dashed blue), temperature in degrees Celsius (orange), depth in meters (purple), and current velocity in m/s (green) are plotted across calendar date spanning from April 9th to May 9th. The current flow measurements are plotted as vectors, where the length of the vector indicates the current flow velocity and its angle indicates the direction of the flow relative to geomagnetic north. The compass is illustrated in the left of the bottom panel. (b) A zoomed-in view of the last 36 hours of collected data, with the same series as shown in (a). (c) Five selected snapshots of current flow from May 1 at 6:20 AM to 9 AM for two tags, Tag 1 in blue, and Tag 2 in orange. Current flow vectors are shown as in (a), superimposed on a map showing each tag's approximate location. Below each snapshot, a trace of the depth in meters recorded by Tag 1 is shown, with a dot indicating the snapshot time. (d) A selected 72 hour segment of depth measurements from Tag 1 in blue, and Tag 2 in orange spanning from April 29th to May 2nd plotted on the left axis. The mean lower-low water level (in meters) measured by a nearby NOAA Tides and Currents Station [22] is plotted on the right axis, relative to Mean Water Low-Level. (e) Monthly temperature distributions from Aug 2025 to Jan 2026 collected from a preliminary tag deployed in the Charles River. Medians are indicated by the horizontal line, with boxes showing the 25th-75th percentile range, and whiskers indicating the full range.

values are highly correlated in time, with a fixed 0.5 m offset due to differences in seabed depth at the two deployment locations. Additionally, water level data gathered from NOAA Tides and Currents Station 8447930 [22] is plotted on the right axis. The traces' similarities highlight the accuracy and time-alignment of our system.

Fig. 2.1e plots monthly temperature distributions collected from a prototype of BlueTag that collected data in the Charles River from Aug 2025 to Jan 2026. Over the course of the 6-month span, the tag measured temperatures fall by roughly 25°C. In January, measured temperatures were just above freezing, with a median temperature of 0.72°C.

Overall, this work represents a more than 60× improvement in the experimental deployment lifetime when compared with state-of-the-art backscatter systems that were only deployed for at most half a day [9,12,13,16–18]. Moreover, our tags can operate and collect data beyond the data windows illustrated here. Specifically, they can last approximately two years before depleting their batteries. Our deployment represents the first underwater backscatter sensing system to collect accurate underwater data from the ocean, demonstrating that our method can support high quality ocean science over extended periods of time using underwater backscatter.

Chapter 3

Approach

3.1 Energy efficient sensing and computing

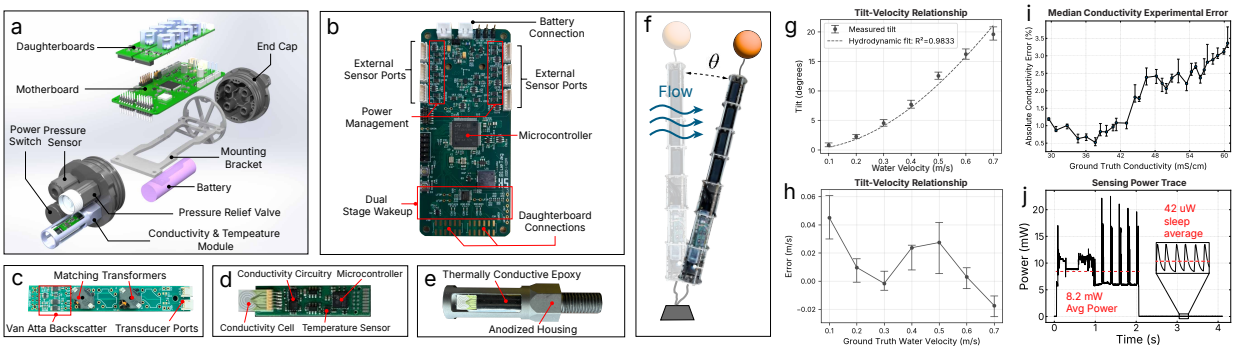

Figure 3.1: **Developed hardware and sensor characterizations.** (a) Exploded view of the assembly of our design. (b) Motherboard PCB. (c) Daughterboard PCB. (d) Conductivity module PCB. (e) Encapsulated conductivity module. (f) Current flow sensing principle. Current flow deflects the tag at some angle θ, which is measured by an accelerometer. (g) Experimental relationship between tag tilt vs. ground truth current velocity. Points represent trial medians, with error bars indicating the 75th and 25th percentiles. The curve (dotted) shows the derived analytical model fit to the observed data. (h) Median current velocity prediction error of new experimental data vs. ground truth velocity. Error bars indicate the 75th and 25th percentiles. (i) Median percent absolute conductivity error (%) vs. ground truth conductivity (mS/cm). Error bars indicate the 75th and 25th percentiles. (j) Instantaneous power consumption (mW) of the tag's sensing cycle plotted vs. time (seconds). In sleep, the tag consumes only 42 μW of power.

In order to be amenable to long-term deployments (multiple years and beyond), our tag must consume as little power as possible while still delivering accurate and reliable sensing. More importantly, our goal is to deliver sensing at regular intervals to enable high quality ocean science. To achieve this, we leverage an energy efficient sensing and memory architecture based on an ultra-low-power microcontroller that minimizes the active processing time and logs data to nonvolatile memory for future offloading.

The tag's default operating mode is an ultra-low-power sleep state. Every 15 minutes, the tag wakes up, records measurements from its four sensors (conductivity, temperature, depth, and water flow direction and magnitude), logs them to memory, and goes back to sleep. Our tag has a capacity of 1,250 sets of these four measurements, each called a *report*, corresponding to roughly 13 days of data at a 15 minute wakeup interval. Each of the sensors are power-gated when inactive, ensuring that they are powered off during the sleep state. Fig. 1.1a illustrates our integrated design. Four acoustic transducers at the top couple the acoustic and electrical domains. An anchor mounts to the bottom of the tag that holds it in place on the seabed. A buoyant float mounts to the top of the tag keeping it upright in the water. An exploded view of the enclosure is illustrated in Fig. 3.1a, showing the internal electronics and the battery.

We measured the power consumption of our design by measuring current consumption during the sensing and sleep states (see Methods). Fig. 3.1j plots the instantaneous power consumption in mW vs. time in seconds of the sensing cycle. At the beginning, the power spikes when the microcontroller wakes from sleep. Then, starting at roughly 800 ms, it samples the four sensors, where the large spikes correspond to I^2C and SPI bus accesses to each sensor. Finally, the power drops when the tag goes back into its sleep state. During this cycle, the tag consumes about 16.4 mJ over the course of 2 seconds, corresponding to an average sensing state consumption of about 8.2 mW. The inset of Fig. 3.1j illustrates the tag's sleep state consumption of roughly 42 µW. The spikes in the sleep state power consumption are due to the pulse frequency modulation mode of the buck converter that provides the main power supply to the motherboard.

3.1.1 CTD Sensing

Our design incorporates two externally housed modules that contact the water to realize conductivity, temperature, and depth sensing. The first is an integrated module based on a custom PCB that measures conductivity through a commercially available 4-point cell [25]. The module drives an AC current through two electrodes and measures the voltage produced at the other two electrodes to measure conductivity. An integrated circuit mounted on the PCB measures temperature that delivers an accuracy of ±0.1°C [26]. The entire module (excluding the terminals of the conductivity electrodes) is potted in thermally conductive epoxy and mounted in a custom housing that interfaces with the main enclosure. The second module is a commercially available sensor that measures pressure up to 10 bar [27]. This sensor delivers an accuracy of ±0.15% of its full scale, corresponding to ±15 mbar. Using the current ambient air pressure at the base station and an estimate of the water density, depth can be computed.

To validate the accuracy of the conductivity sensor design, we measured its response compared to a referee meter [28] that achieves ±2% accuracy. We measured the response of both our design and the referee meter under various potassium chloride solutions, delivering conductivities ranging from 30 mS/cm to 60 mS/cm (see Methods). These values capture a wide range of expected conductivities seen in the ocean [29]. Fig. 3.1i plots the measured median absolute percent conductivity error vs. the referee meter's response in mS/cm. Because high conductivities exhibit a low voltage response at the voltage sense terminals of the conductivity cell, the measured error gradually increases with the solution's ground truth

conductivity. However, our design achieves a median error across the full 30 mS/cm to 60 mS/cm of roughly 2% when compared to the referee meter.

3.1.2 Current Flow Sensing

Underwater current flow is typically measured with acoustic sensors, such as acoustic doppler current profilers (ADCP) [30,31]. Unfortunately, these sensors require transmitting high-power signals into the water, which would quickly drain our design's battery life. To measure current flow at much lower power consumption, we estimate current by measuring the tag's tilt as shown in Fig. 3.1f, induced by drag created when water flows over the tag's body. Due to the availability of small, low-power accelerometers, measuring velocity by this method is well suited for long-term deployments. In addition to the tilt, we also measure the direction that the tag is pointing (its heading relative to magnetic north) using an onboard magnetometer.

We characterized the relationship between the tag's tilt and current velocity experimentally (see Methods), and used it to estimate water velocity for deployed tags. Parameters such as the tag's drag and the buoyancy of the tag's float control the sensitivity of the tilt-velocity relationship and can be tuned to match the expected environmental conditions. Fig. 3.1g plots the tag's tilt in degrees vs. the ground truth flow velocity in m/s. At low flow velocities, the tag tilts by only a few degrees. As the flow velocity increases, the tilt increases nonlinearly, reaching a median tilt of 20 degrees at 1 m/s. We fit a curve matching a simplified analytical model (see Methods) to this experimental data, and use this curve to estimate the flow velocity during deployment. We also characterized the measurement error of this approach by testing its performance against new experimental data (see Methods), illustrated in Fig. 3.1h. Velocity prediction achieves a median absolute error of 0.016 m/s over the tested range.

3.2 Asynchronous data extraction

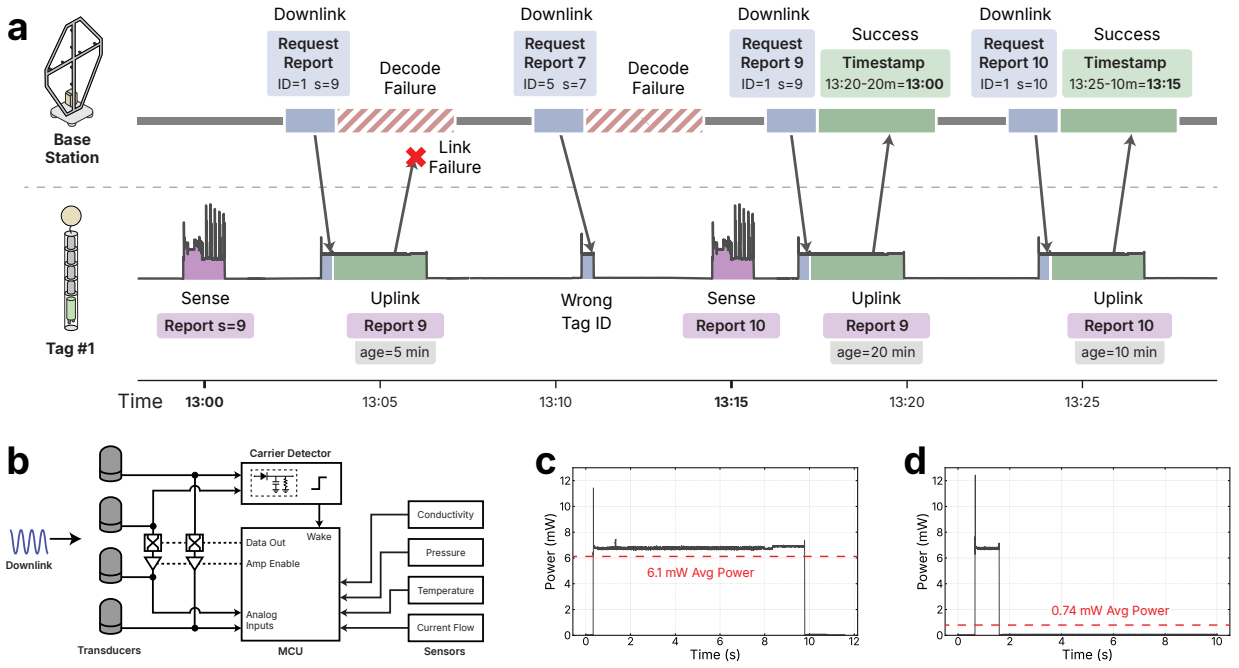

Figure 3.2: **Asynchronous wireless sensing.** (a) Phases of the interactions between the base station (top) and the tag (bottom) plotted across time. At the bottom left in green, tag ID=1 wakes up and collects measurements into a report with sequence number 9, then goes back to sleep. Then, the base station requests sequence number 9 from tag ID=1 by transmitting a downlink command. Tag ID=1 wakes up, inserts report 9's age of 5 minutes in the response, and attempts to uplink this data to the base station. The base station fails to decode this response because of a link failure. The next request for report 9 from tag ID=1 succeeds (after a downlink request to a different tag), and the base station uses the new age (20 minutes) in the response to calculate when report 9 was actually taken (13:00). This process repeats until the base station is fully up to date with the tag's reports. (b) Block diagram of the dual-stage wakeup mechanism. Four transducers are connected in two pairs. The downlink command's envelope is detected by the carrier detector, which wakes the microcontroller from its sleep state. Then, the microcontroller enables the two amplifiers whose outputs feed into the ADC of the microcontroller, which are used to sample and decode the downlink. Finally, data previously collected from the sensors is transmitted by modulating the polarity of each pair's connection. (c) Instantaneous power consumption (mW) plotted vs. time (seconds) for a successful downlink wakeup and uplink (backscatter) cycle. (d) Instantaneous power consumption (mW) plotted vs. time (seconds) for a false downlink wakeup, where the tag successfully decodes a downlink command that was intended for a different tag ID. In this case, the tag simply ignores the command and goes back to sleep.

A key goal of our design is to be able to capture and offload frequent, regularly spaced sensor measurements from the environment. Recall that our design captures sensor data every 15 minutes and stores those measurements in its onboard memory as a *report*. However, this data is inaccessible unless we can offload it to the surface. To achieve this, our design leverages underwater backscatter to transmit this report from the tag to the base station. Specifically, we implement a four element Van Atta array of backscatter transducers as described in previous work [18]. This transmission is called the *uplink*.

Another goal of our design is for the base station to be able to coordinate with and offload data from multiple tags deployed in the environment. This means we need to be able to individually query different tags, and selectively request their measurements when we need them. To achieve this, our design uses a base station-mediated time-division multiple access (TDMA) approach, where the base station transmits commands that contain a unique tag identifier (ID) to a specific tag in the environment. This command requests reports from the tag, and is known as the *downlink*.

However, in order to decode commands from the base station on the tag, we need an embedded decoder that can parse these commands. Such a decoder must remain ready to receive downlink commands because a request from the base station may arrive at any time. A naive approach would be to use an analog-to-digital converter (ADC) to constantly sample acoustic signals at the transducers, but this would waste the tag's battery life when no base station downlink commands are occurring.

To overcome this, our design leverages a *dual-stage wakeup* mechanism that attempts to decode downlink commands based on two key criteria. To understand this, consider Fig. 3.2b. In the first stage, an ultra-low-power envelope detector constantly listens for acoustic signals at the transducers. If it detects signals above a certain strength, it outputs a digital high signal that is used to wake up the microcontroller. In the second stage, the microcontroller samples the acoustic signal with an onboard ADC and attempts to decode the downlink command (see Methods). This decoding process searches for the tag ID in the downlink packet header, and responds by transmitting the report (the sensor data) only if the tag ID matches a pre-programmed value stored onboard the microcontroller. The envelope detector maintains a power consumption of roughly 6 μW while active, enabling the microcontroller and its onboard ADC to remain inactive while asleep yet responsive to downlink commands when they appear.

We measured the power consumption of this downlink decoding process by probing a current trace both when the correct tag ID is sent and an incorrect tag ID is sent. During the first case, as shown in Fig. 3.2c, the tag consumes about 64.1 mJ over the course of 10.5 seconds, corresponding to an average successful decode state power consumption of about 6.1 mW. The power consumption remains high until about 10 seconds because the tag is backscattering uplink data. During the second case, as shown in Fig. 3.2d, the tag consumes about 6.9 mJ over the course of 9.3 seconds, corresponding to an average power consumption of about 0.74 mW. Here, the power consumption drops after about a second, because the tag decoded a command that was intended for a different tag, and returns to sleep without backscattering uplink data.

3.2.1 Data and time synchronization

When the acoustic channel becomes poor for extended periods of time, it is possible for the tag to sample many reports that the base station fails to decode on the uplink. The base station may be unaware of these reports, but the data itself is not lost because tags store these reports in a rolling buffer in memory. To access this data, the base station must be able to selectively ask for specific reports that were captured in the past so that it can backfill missing data. Importantly, the base station needs an accurate understanding of when these reports were taken in time so that a sequence of reports will accurately reflect the true environmental conditions over time.

Theoretically, tags could append an absolute timestamp to each report uplink for the base station to decode. Unfortunately, all clocks drift, and more importantly, we need a clock solution onboard our tag that is aligned with our primary ultra-low-power design goal. Even commercially available chip-scale atomic clocks would consume hundreds of milliwatts of power [32,33]. We could solve this problem by periodically synchronizing the tag, similar to protocols like NTP or PTP [34–36], but this solution would consume valuable network capacity that is already constrained, and would worsen linearly with the number of tags in the network.

To address these challenges and enable the base station to access historical data, we augment a tag's reports with a value called a *sequence number*. The sequence number is a monotonically increasing identifier that the base station and tag use to reference reports. This number is initialized to zero when the tag is power cycled. To understand how this works, consider Fig. 3.2a. If the base station has received reports from a tag with sequence numbers: $s-2$, $s-1$ and $s+1$, it can identify that sequence number s is missing and specifically request it from a tag. To do so, the base station forms a downlink command that addresses a specific tag ID and report sequence number. When the addressed tag decodes this downlink command, it returns the report corresponding to that sequence number in its uplink.

To enable the base station to learn when a report was captured without periodic time synchronization, we augment the tag's uplink with an additional value called a *report age*. Intuitively, this number represents how "old" the report is. To understand this, Fig. 3.2a illustrates the sequence of events upon a base station request for a report. When the tag successfully decodes a downlink command requesting a specific sequence number, the tag marks its absolute time. Then, the tag computes the *difference* between this time and the absolute time when the requested report was captured, and places this number into its uplink response. When the base station receives this uplink, it subtracts the report age from its own network time (provided by NTP) to calculate the time at which the measurement was actually taken. This approach enables each tag to be equipped with a real-time clock (RTC) that is driven by a low power 32.768 kHz crystal.

In our design, this crystal achieves an accuracy of ± 5 ppm [37], corresponding to a rate of roughly 1 second every 2.3 days. However, because the report age is differential in nature, this drift will not accumulate with run time, setting an upper bound on the maximum report time error of roughly 5.6 seconds. This assumes that the acoustic link fails for the entire 13 days of report storage onboard our tag, which is extremely unlikely based on our experimental analysis. Beyond this size, the buffer overflows and data older than 13 days is lost.

3.3 SNR-aware adaptive backscatter networking

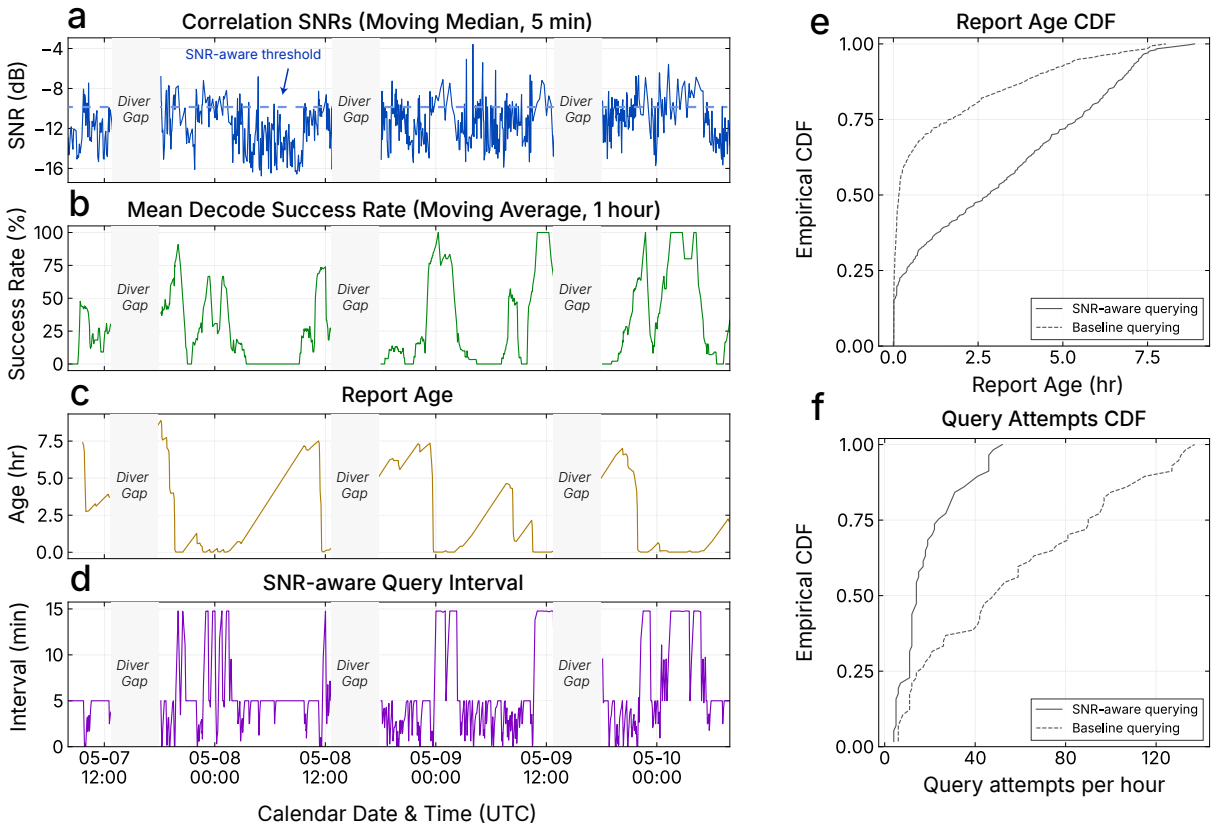

Figure 3.3: **Network metrics for a single sensor.** (a) Correlation signal-to-noise ratios (dB) vs. calendar date. The data is filtered with a moving median filter of window size equal to 5 minutes, which is the same window used in our adaptive querying technique. The blue dotted line indicates the -10 dB threshold for backing off or accelerating the rate of queries. In the following subfigures, the gray rectangles indicate the forced inactive time of the base station during which the Woods Hole divers are in the water. (b) Mean decode success rate (%) vs. calendar date. The data is filtered with a moving average filter of window size equal to 1 hour. (c) Report age (hours) vs. calendar date. (d) Polling interval (minutes) vs. calendar date. (e) CDF of the report ages in hours. (f) CDF of the number of query attempts per hour.

In a network of deployed tags, acoustic channel conditions vary with both time of day and tag position relative to the base station. As a result, uplink reliability varies across tags: reports from nearby tags are received, on average, with higher signal strength and higher success rates than reports from farther tags. Meanwhile, every downlink command that the base station transmits is detected by all tags in the network; because the first stage of our dual-stage wakeup mechanism is detecting the downlink signal strength, any downlink command incurs the power cost of waking up and attempting to decode *at all tags*, regardless of whether that command was intended for that tag.

These challenges create a tradeoff between two competing objectives. First, the base station must limit how frequently it queries the network, since excessive downlink commands incur a cumulative power cost on all tags in the network. Second, if the base station must backfill missing data from a tag and the acoustic link is strong, it should request tag reports more frequently to gain timely knowledge of both the current and historical environmental conditions.

To address these challenges, we introduce an *SNR-aware* adaptive querying technique that queries the tags at a rate determined by the current channel conditions. Intuitively, this means that when a link is strong, the base station queries a tag more often in the hopes that most of its requests will succeed. If the link is poor, the base station queries less often, since we expect decodes to fail. Our approach uses the correlation signal-to-noise ratio (SNR) of a 512-bit training sequence at the start of the uplink response (see Methods) as an indicator of the current channel conditions. If the median of the last five minutes of correlation SNRs is below a fixed threshold, we linearly increase the time interval that the base station will wait before the next query. If the median of the last five minutes of correlation SNRs is larger than this threshold, we decrease this time interval by a multiplicative factor. We fix the minimum interval to zero, and the maximum interval to the tag's measurement cadence divided by three (5 minutes). If the base station is fully up-to-date, it waits until it expects the next sample to have been captured on any given tag.

During periods of poor acoustic channel conditions, this approach backs off the base station downlink commands to prevent excessive power consumption at all the tags in the network. When the acoustic channel returns to a stronger state, the base station begins filling in missing tag data, and opportunistically queries the tag faster to retrieve this data. In a network of tags, the base station keeps track of this querying interval for each tag independently. In the event of scheduling conflicts, the base station prioritizes the tag whose most recently offloaded report is older.

Fig. 3.3 illustrates a set of four metrics (correlation SNR, mean decode success rate, report age, and query interval) plotted across calendar date from May 6, 2026 to May 9, 2026 from a single deployed tag. These metrics collectively demonstrate the performance of our adaptive querying technique. The gray boxes in subfigures (a) through (d) represent times when the base station was inactive. We intentionally turn the base station off during these grayed-out periods because we do not want to transmit acoustics into the water when the divers are below the surface.

First, Fig. 3.3a shows the correlation SNRs over this time period. This correlation SNR is a measure of the quality of the acoustic link, and varies between -16 dB and -3 dB. The SNR is negative because our correlator outputs a normalized value (maximized at 0 dB). The SNR varies significantly within the illustrated range, fluctuating at both small and large time scales. For example, on the early morning of May 8, the SNR was relatively low, but as the day continued, it grew stronger and occasionally exceeded our threshold.

Fig. 3.3b plots the mean decode success rate over the same time period, filtered with a one-hour moving average. The success rate closely tracks the correlation SNR shown in Fig. 3.3a: during periods when the SNR drops well below the -10 dB threshold, the success rate falls sharply, at times reaching nearly 0%. Conversely, when the SNR rises above the threshold, the success rate recovers rapidly, often exceeding 75% within a short window. This tight correlation demonstrates that correlation SNR is a useful proxy for link quality and that

our querying strategy quickly adapts when the channel can support reliable communication.

Fig. 3.3c plots the report age, defined as the time elapsed between when a report was captured and when it was successfully received at the base station. During periods of strong SNR and high decode success rate, the report age remains near zero, indicating that the base station is retrieving data almost as soon as it is measured. However, during extended periods of poor channel conditions, the report age grows as reports accumulate on the tag without being offloaded. Importantly, when the channel recovers, the report age drops sharply as our algorithm accelerates its query rate and the base station rapidly backfills the missing data. Note that the report age always grows during the diver gaps, since the base station is inactive during these periods.

Fig. 3.3d plots the SNR-aware query interval in minutes over the same time period. When the channel is poor, the adaptive algorithm increases the interval between successive queries, reaching a maximum of 5 minutes during the worst channel conditions. This backoff reduces the cumulative power cost on the network of tags, yet keeps knowledge of the link quality up-to-date by attempting to retrieve data at least 3 times during the tag's 15 minute measurement window. When the SNR rises above the -10 dB threshold, the interval decreases rapidly due to the multiplicative decrease rule, dropping to near zero within minutes. Note that the increase in this query interval beyond 5 minutes represents periods when the base station is nearly in sync with the tag, because it must wait some time before the tag captures a new measurement.

Fig. 3.3e plots the empirical cumulative distribution function (CDF) of the report ages. The y-axis of this plot represents the fraction of observations that fall at or below a given report age on the x-axis. The median report age is roughly 3 hours and 45 minutes, and the 90th percentile report age is roughly 7 hours. The long tail extending to approximately 7.5 hours corresponds to rare periods of sustained poor channel conditions. These ages are sufficiently smaller than the 13 days of report buffer size, leaving ample room for future anomalous periods of poor link conditions.

Finally, Fig. 3.3f plots the empirical CDF of the number of query attempts per hour. The median is roughly 15 attempts per hour, and the 90th percentile is roughly 45 attempts per hour. The tail extends slightly beyond 45 attempts per hour, corresponding to bursts of rapid querying when the base station is backfilling accumulated reports after a channel recovery. At the lower end, periods with fewer than 10 queries per hour correspond to intervals when the adaptive algorithm has backed off due to poor SNR.

Chapter 4

Conclusion

This thesis presented BlueTag, an underwater backscatter tag and base station for long-term, networked ocean sensing. By tightly coupling ultra-low-power sensing with a dual-stage wakeup, asynchronous data extraction, and an SNR-aware adaptive querying strategy, the system enables untethered, distributed subsea monitoring for years of operation. A month-long coastal deployment in Woods Hole, Massachusetts confirmed the system's ability to collect accurate measurements from a network of tags despite channel variability. The collected data resolved daily and lunar tidal cycles, spring-tide amplitude maxima, and spatially-coherent flow patterns consistent with the known hydrodynamics of the harbor. The deployment represents a more than 60× improvement in experimental duration over prior underwater backscatter systems, with a projected per-tag lifetime of approximately two years. Future work involves scaling these results to larger networks with additional sensing modalities to enable the persistent observation of subsea infrastructure, ocean ecosystems, and climate processes.

Chapter 5

Methods

5.1 Tag Implementation

Construction. Four BT-2RCL acoustic transducers [38] comprise the backscatter array. Cables connect this array to the electronics housing, which is a 2 inch BlueRobotics Watertight Enclosure [39]. The cables penetrate the enclosure via BlueRobotics M10 7.5mm WetLinks [40]. A custom 3D printed bracket holds the motherboard in the center of the tube. Laser-cut aluminum plates and aluminum standoffs comprise the cage that supports and protects the transducers. A shackle at the top of the cage connects to a float providing approximately 7 lbs of buoyancy. On the bottom, another shackle connects to a 15 lb anchor. To avoid galvanic corrosion between cage and stainless steel hardware, a sacrificial zinc anode is mounted to each tag.

Motherboard. The microcontroller of the motherboard is an STM32U535 chip [41]. There are six external sensor ports, two that support SPI sensors and four that support I^2C sensors. Power gating at each sensor port is realized with the TPS22917 chip [42]. The first stage of the dual stage wakeup mechanism is implemented with the AS3933 chip [43]. Upon detecting an acoustic signal at one of the transducers, it triggers an edge that repeats every 50 milliseconds for as long as a carrier is present. This edge wakes the microcontroller from sleep.

Daughterboards. Backscatter uplink communication is realized via a semi-passive Van Atta array with 20 dB of amplifier gain, as described in prior work [18]. Impedance matching transformers convert the transducer impedances to a real 2 kΩ value.

Conductivity and Temperature Module. The conductivity subsystem drives a 200 Hz sine wave into the LFS1107 current drive terminals. An instrumentation amplifier amplifies the voltage at the voltage sense terminals, and a transimpedance amplifier converts the drive current into a voltage. These signals are sampled by the microcontroller's onboard ADC. Then, conductivity is calculated as

$$\sigma = K\frac{I}{V}, \tag{5.1}$$

where I and V are the rms current and rms voltage measured by the ADC, and K is the cell constant of the LFS1107, typically 0.43 cm^{-1}.

The sensor module PCB (illustrated in Fig. 3.1d) is potted using a marine epoxy into a custom aluminum penetrator. Shown in Fig. 3.1e, a layer of thermally conductive epoxy protects the exposed PCB from water, except for the terminals of the conductivity sensor, which are left exposed to the water. Conductivity is converted to specific conductance at 25°C using a 2% per degree celsius temperature dependence [44].

5.2 Base Station Implementation

The base station array consists of one BT2RCL [38] and an 8-element HTI-96-MIN [45] hydrophone array arranged in a cross pattern. Four hydrophones make up the horizontal component and the other four make up the vertical component of the array. The base station frame was fabricated from aluminum and welded together. Weights at the bottom of the base station anchor it to the seabed.

Cables connect the array elements to the base station electronics enclosure. The elements interface with a WHOI Micromodem [46], which provides amplification to the transmit and receive signals. A Raspberry Pi 5 [47] equipped with HifiBerry DAC8x and ADC8x add-on boards [48,49] acts as the digital audio interface. Userspace software written in Python and C performs downlink encoding and transmission, as well as uplink reception and decoding. The base-station software also schedules transmissions and uploads collected data to the Internet.

5.3 Deployment

The base station transducer array was lowered via crane to the seabed. A team of divers maneuvered the base station to its deployed location and pointed it toward the tag deployment area. Cables were routed from the base station to an enclosed shelter above the surface. Tags were placed on the seabed by divers with their complete moorings attached, aided with lift bags. Divers used a predeployed dive line system to approximately position the tags. The base station and tags were all deployed at around 20 meters of depth.

5.4 Packet Structures

Downlink Packets. Downlink packets allow the base station to command a tag to perform an operation. Most commonly they allow the base station to request a sensor data report from a particular tag. Additionally, commands allow the base station to set parameters on the tag, such as the measurement cadence, or which sensors are enabled. Due to the difficulty in retrieving tags, these are helpful to reconfigure the sensor network once deployed. Downlinks begin with a byte indicating the *tag ID* and a byte for the *protocol version*, which are used by a tag to filter requests for other devices. Then a byte indicates the *command type*, followed by a variable length *command payload*. For example, the *get report* command has a 4 byte payload for a *sequence number* to request a specific report from a tag. Finally, a CRC byte ensures accuracy.

Downlink data is modulated using chirp spread spectrum (CSS) with a bandwidth of 4 kHz, centered at 28.8 kHz at 50 bits per second. Upchirps phase-shifted by 0 and 180 degrees

represent bits 0 and 1 respectively. Tags implement a sub-Nyquist decoder architecture, sampling at 12.8 kHz, that reduces the power consumption of downlink processing [16].

Uplink Packets. Uplink packets carry either acknowledgments to downlink commands or sensor reports requested by the base station. Each uplink begins with a one byte *byte count*, which specifies the total number of decoded bytes in the packet, used to inform the decoder about the payload size. This is followed by a one byte *tag ID* and a one byte *packet type*. Acknowledgment packets use a one byte *status* field to indicate success or an error code. Report packets contain an 8 byte *report header*, followed by a variable length sequence of report fields. The report header contains a 32 bit *sequence number*, a one bit flag indicating whether this is the latest available report, and a 31 bit report age in seconds. Each report field is encoded as a one byte field key followed by a fixed-size integer or float value.

Uplink data is modulated using FM0 encoding at a rate of 512 symbols per second. Each uplink packet begins with 512 symbols of a pseudorandom sequence (used for locating and training) followed by the uplink's data. To improve resilience to bit errors, the tag encodes every 16 bytes of the uplink packet into a 1024-symbol polar-encoded block, resulting in a 1/8 coding rate. Uplinks are decoded by the base station using a decision feedback equalizer (DFE), to estimate and track the channel [20].

5.5 Water Flow Sensing

To measure water flow at low power, tags estimate water velocity from drag-induced tilt relative to vertical. Each tag includes an ADXL366 accelerometer to measure tilt [50]. Assuming gravity is the only acceleration, the tilt angle, θ, is the angle between the measured acceleration vector, $\mathbf{a}$, and the vertical axis, $\hat{\mathbf{v}}$:

$$\theta = \arccos\left(\frac{\mathbf{a}\cdot\hat{\mathbf{v}}}{\|\mathbf{a}\|}\right). \tag{5.2}$$

Tags also include an MMC5603 magnetometer [51] to estimate heading, defined as the compass direction of the tag's tilt. To find heading, we first project the measured magnetic field, $\mathbf{m}$, onto the horizontal plane to obtain magnetic north,

$$\mathbf{m}_h = \mathbf{m} - (\mathbf{m}\cdot\hat{\mathbf{v}})\hat{\mathbf{v}}, \qquad \hat{\mathbf{n}} = \frac{\mathbf{m}_h}{\|\mathbf{m}_h\|}, \tag{5.3}$$

and define east as

$$\hat{\mathbf{e}} = \hat{\mathbf{n}}\times\hat{\mathbf{v}}. \tag{5.4}$$

Let $\hat{\mathbf{t}}$ be the unit vector along the tag axis. Projecting it onto the horizontal plane gives

$$\mathbf{t}_h = \hat{\mathbf{t}} - (\hat{\mathbf{t}}\cdot\hat{\mathbf{v}})\hat{\mathbf{v}}. \tag{5.5}$$

The tag heading, ψ, is then

$$\psi = \operatorname{arctan2}(\mathbf{t}_h\cdot\hat{\mathbf{e}},\ \mathbf{t}_h\cdot\hat{\mathbf{n}})\,. \tag{5.6}$$

Simplified Analytical Model. Consider a model of the tag subject to gravity, buoyancy, drag from the current, and rope tension, denoted by f_{grav}, f_{buoy}, f_{drag}, and f_{rope}, respectively. In steady state, the vertical and horizontal forces balance, giving

$$f_{buoy} - f_{grav} = f_{rope} \cos\theta, \tag{5.7}$$

$$f_{drag} = f_{rope} \sin\theta. \tag{5.8}$$

Solving yields

$$f_{drag} = (f_{buoy} - f_{grav}) \tan\theta. \tag{5.9}$$

f_{drag} is a function of physical properties of the tag and water, K, times the water velocity squared, v^2. Solving for v gives

$$v = \sqrt{\frac{(f_{buoy} - f_{grav}) \tan\theta}{K}}. \tag{5.10}$$

Importantly, this relationship assumes that the tag's drag constant, K is constant with orientation, which we find to be a reasonable approximation for small-angle tilts. To find the remaining unknown constants, we empirically measure the tag's response to different water flow velocities and use a least-squares regression to solve for the quantity $\frac{f_{buoy}-f_{grav}}{K}$.

Characterization of Tilt-Velocity Relationship. We perform controlled experiments in a pool to measure a tag's tilt under different water velocities. Experiments are conducted in two rounds, first to calibrate our system, solving for unknown values in the tilt-velocity relationship, and then to evaluate the accuracy of tilt-based water flow estimation.

For each, the tag is moved through the water at various fixed speeds while data from the tag's accelerometer is recorded. As shown in Fig. 5.1, the tag is secured at its bottom shackle to an aluminum boom with rope. The aluminum boom is mounted to a sliding cart, riding on a track fixed to the edge of the pool. A motorized pulley moves the cart, boom and tag through the water, causing the tag to experience an identical force to water flowing around the tag. A UART connection to the tag's microcontroller allows us to log accelerometer data during each trial. For both calibration and evaluation rounds, we perform 10 trials at speeds ranging from 0.1 m/s to 1.0 m/s.

To calibrate our flow estimation, we fit the analytical model to the calibration data. We use this relationship, shown in Fig. 3.1g, to compute the flow for a given tilt angle. The accuracy, shown in Fig. 3.1h, is then the error between the true movement speed of the tag and the measured flow speed for trials in the evaluation data set.

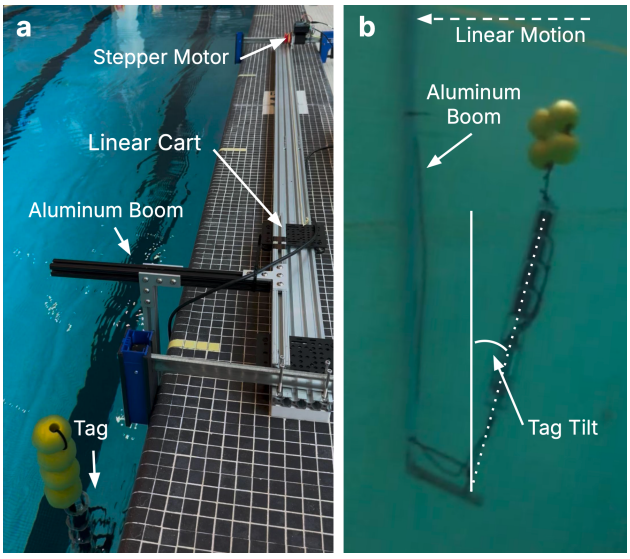

Figure 5.1: **Tilt-velocity characterization and evaluation.** (a) The flow-velocity experimental setup is pictured. The tag is dragged through the water by its bottom shackle at a number of fixed velocities by a motorized cart. A motorized pulley moves the cart, boom and tag through the water, causing the tag to experience an identical force to water flowing around the tag. (b) The tag is moved through the water at various fixed speeds inducing a tilt angle on the tag.

5.6 Disruption-tolerant querying

The SNR-aware control algorithm that determines the interval for which the base station waits before querying a tag again is specified in Algorithm 1. We use $\alpha = 30$, $W = 300$ seconds, $T_{\text{max}} = 300$ seconds, $T_{\text{default}} = 900$ seconds, and the SNR threshold (S_0) as -10 dB. We choose -10 dB because we empirically find that the link has a substantially higher chance of succeeding above this value.

The baseline querying algorithm that we compare our SNR-aware technique to is specified in Algorithm 2. This algorithm queries each tag as fast as possible, regardless of the recent correlation SNRs. If the base station is up-to-date, this algorithm waits until the next measurement from a tag is expected to be captured.

The function TimeUntilNextReport() returns the most recently received report's timestamp (computed from report age) plus the known measurement cadence minus the current wall clock time. When this value is positive, the base station is fully up-to-date. When this value is negative, the base station is behind on reports.

5.7 Lifetime Analysis

There are five key stages of operation on the tag, each of which consume different power levels. These are: sleep, sensing, downlink success and backscatter, downlink wrong ID, and downlink false wakeup. We estimate the lifetime of the tag by estimating the total average

Algorithm 1 SNR-aware adaptive query interval control

Require: Tag ID i
Require: SNR threshold S_0
Require: Backoff coefficient α
Require: SNR lookback window W (seconds)
Require: Maximum interval $T_{\max}$
Require: Measurement cadence T_{default}
Ensure: Next polling interval T_{next} (seconds)

$T_{\text{cur}} \leftarrow \textsc{GetPollingInterval}(i)$

if $\textsc{BaseStationIsUpToDate}(i)$ **then**
  $T_{\text{next}} \leftarrow \max\Big(0,\ \textsc{TimeUntilNextReport}(i) + 30\Big)$
  return T_{next}
end if

$\mathbf{s} \leftarrow \textsc{GetRecentCorrelationSNRs}(i, W)$
if $\mathbf{s} = \emptyset$ **then**
  $T_{\text{next}} \leftarrow T_{\text{cur}}$
  return T_{next}
end if

$s_{\text{med}} \leftarrow \text{median}(\mathbf{s})$
if $s_{\text{med}} > S_0$ **then**
  $T_{\text{next}} \leftarrow T_{\text{cur}}/2$
else
  $T_{\text{next}} \leftarrow T_{\text{cur}} + \alpha \cdot (S_0 - s_{\text{med}})$
end if

return $\min(\max(T_{\text{next}}, 0), T_{\max})$

Algorithm 2 Baseline query interval control

Require: Tag ID i
Require: Measurement cadence T_{default}
Ensure: Next polling interval T_{next} (seconds)

if $\textsc{BaseStationIsUpToDate}(i)$ **then**
  $T_{\text{next}} \leftarrow \max\Big(0,\ \textsc{TimeUntilNextReport}(i) + 30\Big)$
else
  $T_{\text{next}} \leftarrow 0$
end if

return T_{next}

Table 5.1: **Current and charge consumption analysis.** Current consumption for each stage (I_s), and the corresponding stage duration (t_s), entry count (n_s), and total stage charge (Q_s) for tags 1 and 2 under the SNR-aware adaptive querying strategy. On the right, the same information is listed under the baseline querying strategy. At the bottom are the total charge, total average current, and estimated lifetime for both querying strategies. All metrics are per 15 minute sensing interval.

		SNR-aware adaptive querying						**Baseline querying**					
		Tag 1			**Tag 2**			**Tag 1**			**Tag 2**		
Stage	I_s (mA)	t_s (s)	n_s	Q_s (mC)	t_s (s)	n_s	Q_s (mC)	t_s (s)	n_s	Q_s (mC)	t_s (s)	n_s	Q_s (mC)
Sleep	0.011	800	1	8.90	797	1	8.87	601.5	1	6.69	593.6	1	6.61
Sensing	2.21	2.01	1	4.44	2.01	1	4.44	2.01	1	4.44	2.01	1	4.44
Downlink success	1.65	10.5	3.69	64.0	10.5	5.57	96.6	10.5	11.22	194.4	10.5	18.32	317.4
Downlink wrong ID	0.2	9.35	5.57	10.44	9.35	3.69	6.92	9.35	18.32	34.3	9.35	11.22	21.0
Downlink false wakeup	1.82	0.77	10	14.0	0.77	10	14.0	0.77	10	14.0	0.77	10	14.0
Total Charge (mC)		**101.83**			**130.83**			**253.9**			**363.5**		
Total Average Current (mA)		**0.11**			**0.15**			**0.28**			**0.40**		
Lifetime (years)		**2.52**			**1.96**			**1.01**			**0.71**		

charge consumed over the core 15 minute sensing interval. This lifetime is given by:

$$L = \frac{CT}{Q} \tag{5.11}$$

where L is the tag lifetime in hours, C is the battery capacity in milliamp-hours ($C = 2500$ mAh), Q is the estimated charge consumed per 15 minute cycle, and T is sensing cadence in seconds ($T = 900$ s). The total charge is the sum of each stage charge:

$$Q = \sum_s Q_s \tag{5.12}$$

where Q_s is each stage charge, $s = 0$ represents the sleep stage, $s = 1$ represents the sensing stage, $s = 2$, represents the downlink success and backscatter stage, $s = 3$ represents the downlink wrong ID stage, and $s = 4$ represents the downlink false wakeup stage. The downlink false wakeup stage is distinct from the downlink wrong ID stage, and occurs when nearby acoustic transmissions or noise is heard by the carrier detector on our tag. This wakes the tag, but does not form a proper downlink command, so the tag ignores it. Based on our evaluation, this stage consumes about 5.2 mJ over 0.77 seconds. In practice, we see that this false wakeup phenomenon happens at a rate of about 10 times per 15 minute measurement cadence.

To compute each stage charge, we use the measured power consumption and time values described in the previous sections, and multiply this charge by the estimated number of times the tag enters this stage. Specifically:

$$Q_s = I_s t_s n_s \tag{5.13}$$

where I_s is the average current consumption (mA) for each stage, t_s is the duration (s) for each stage, and n_s is the entry count for each stage.

The sleep charge (Q_0) is dependent on the number of times the other stages are entered, thus we compute it as:

$$Q_0 = I_0(T - \sum_{s \neq 0} t_s n_s) \tag{5.14}$$

Since the sensing stage is entered only once per 15 minutes, $n_1 = 1$. To estimate the downlink success + backscatter (n_2) and downlink wrong ID (n_3) entry counts, we compute the mean query attempts per 15 minute cycle for each tag from our deployment data. Because all tags in the network hear all downlink requests, n_3 for each tag is the sum of n_2 across all other tags in the network.

Table 5.1 summarizes the breakdown of current, time, and charge per stage for each tag with our SNR-aware querying strategy, and compares it to the baseline strategy. Notably, for our adaptive strategy, the mean entry count per 15 minute interval for the downlink success and downlink wrong ID stages is significantly less than the baseline. This is because our strategy backs off queries when the channel is poor, significantly reducing the number of times the base station transmits downlink commands, and correspondingly reduces the amount of charge consumed by each of these stages on each tag in the network. The baseline strategy yields an estimated lifetime of roughly 1 year for tag 1 and only about 8.5 months for tag 2. On the other hand, our adaptive strategy yields an estimated lifetime of roughly 2.5 years for tag 1 and 2 years for tag 2, representing a more than 2.5× improvement in lifetime across both tags.

References

[1] NOAA Pacific Marine Environmental Laboratory. *Observations and Data*. https://www.pmel.noaa.gov/co2/story/Observations%2Band%2BData. Accessed: 2026-05-09.

[2] N. Lo Bue et al. "The Importance of Marine Research Infrastructures in Capturing Processes and Impacts of Extreme Events." *Frontiers in Marine Science*, 2021. DOI: 10.3389/fmars.2021.626668.

[3] United Nations Conference on Trade and Development. *Review of Maritime Transport 2024*. Tech. rep. Geneva: United Nations, 2024. URL: https://unctad.org/publication/review-maritime-transport-2024.

[4] Food and Agriculture Organization of the United Nations. *The State of World Fisheries and Aquaculture 2024 – Blue Transformation in Action*. Tech. rep. Rome: FAO, 2024. DOI: 10.4060/cd0683en.

[5] B. C. Glavovic, R. Dawson, W. Chow, M. Garschagen, M. Haasnoot, C. Singh, and A. Thomas. "Cross-Chapter Paper 2: Cities and Settlements by the Sea." In: *Climate Change 2022: Impacts, Adaptation and Vulnerability. Contribution of Working Group II to the Sixth Assessment Report of the Intergovernmental Panel on Climate Change*. Ed. by H.-O. Pörtner, D. C. Roberts, et al. Cambridge University Press, 2022, pp. 2163–2194. DOI: 10.1017/9781009325844.019.

[6] C. R. Barnes, M. M. R. Best, L. Pautet, and B. Pirenne. "Understanding Earth–Ocean Processes using Real-time Data from NEPTUNE, Canada's Widely Distributed Sensor Networks, Northeast Pacific." *Geoscience Canada*, **38**(1), 2011. URL: https://journals.lib.unb.ca/index.php/GC/article/view/18588.

[7] J. A. Rice, D. Green, and B. Fletcher. "Seaweb Acoustic Communication and Navigation Networks." In: *Proceedings of MTS/IEEE OCEANS 2001*. 2001.

[8] D. Roemmich, G. C. Johnson, S. Riser, R. Davis, J. Gilson, W. B. Owens, S. L. Garzoli, C. Schmid, and M. Ignaszewski. "The Argo Program: Observing the Global Ocean with Profiling Floats." *Oceanography*, **22**(2), 2009, pp. 34–43. DOI: 10.5670/oceanog.2009.36.

[9] J. Jang and F. Adib. "Underwater backscatter networking." In: *Proceedings of the ACM Special Interest Group on Data Communication*. 2019, pp. 187–199.

[10] L. Freitag, M. Grund, S. Singh, J. Partan, P. Koski, and K. Ball. "The WHOI Micro-Modem: An Acoustic Communications and Navigation System for Multiple Platforms." In: *Proceedings of OCEANS 2005 MTS/IEEE*. IEEE. Washington, DC, 2005. DOI: 10.1109/OCEANS.2005.1639901.

[11] Popoto Modem. *S1000RP — Remotely Powered Slim Acoustic Modem*. https://store.popotomodem.com/products/s1000rp. Accessed: 2026-04-25. 2026.

[12] R. Ghaffarivardavagh, S. Afzal, O. Rodriguez, and F. Adib. "Ultra-Wideband Underwater Backscatter via Piezoelectric Metamaterials." In: *Proceedings of the ACM Special Interest Group on Data Communication*. 2020.

[13] S. S. Afzal, R. Ghaffarivardavagh, W. Akbar, O. Rodriguez, and F. Adib. "Enabling higher-order modulation for underwater backscatter communication." In: *Global Oceans 2020: Singapore–US Gulf Coast*. IEEE. 2020, pp. 1–6.

[14] W. Akbar, A. Allam, and F. Adib. "The Underwater Backscatter Channel: Theory, Link Budget, and Experimental Validation." In: *Proceedings of the 29th Annual International Conference on Mobile Computing and Networking*. 2023, pp. 1–15.

[15] S. S. Afzal, W. Akbar, O. Rodriguez, M. Doumet, U. Ha, R. Ghaffarivardavagh, and F. Adib. "Battery-free wireless imaging of underwater environments." *Nature communications*, **13**(1), 2022, pp. 1–9.

[16] P. Wang, S. S. Afzal, and F. Adib. "Mobile Underwater Backscatter Networking." In: *Proceedings of the ACM SIGCOMM 2025 Conference*. SIGCOMM '25. Convento São Francisco, Coimbra, Portugal: Association for Computing Machinery, 2025, pp. 1025–1039. ISBN: 9798400715242. DOI: 10.1145/3718958.3750507. URL: https://doi.org/10.1145/3718958.3750507.

[17] A. Eid, J. Rademacher, W. Akbar, P. Wang, A. Allam, and F. Adib. "Enabling Long-Range Underwater Backscatter via Van Atta Acoustic Networks." In: *ACM SIGCOMM 2023*. 2023, pp. 1–19.

[18] S. S. Afzal, J. Rademacher, W. Chen, P. Wang, and F. Adib. "Scalable and Low Power Localization for Underwater Robots." In: *Proceedings of the 31st Annual International Conference on Mobile Computing and Networking*. ACM MOBICOM '25. Kerry Hotel, Hong Kong, Hong Kong, China: Association for Computing Machinery, 2025, pp. 1075–1090. ISBN: 9798400711299. DOI: 10.1145/3680207.3765265. URL: https://doi.org/10.1145/3680207.3765265.

[19] P. Qarabaqi and M. Stojanovic. "Statistical Characterization and Computationally Efficient Modeling of a Class of Underwater Acoustic Communication Channels." *IEEE Journal of Oceanic Engineering*, **38**(4), 2013, pp. 701–717. DOI: 10.1109/JOE.2013.2278787.

[20] M. Stojanovic, J. Catipovic, and J. G. Proakis. "Adaptive multichannel combining and equalization for underwater acoustic communications." *The Journal of the Acoustical Society of America*, **94**(3), 1993, pp. 1621–1631.

[21] A. Stefanov and M. Stojanovic. "Communication theoretic analysis of underwater ad-hoc networks in the presence of interference." In: *2010 IEEE Globecom Workshops*. IEEE. 2010, pp. 186–190.

[22] National Oceanic and Atmospheric Administration, National Ocean Service, Center for Operational Oceanographic Products and Services. *NOAA Tides & Currents: Woods Hole, MA – Station ID 8447930*. 2026. URL: https://tidesandcurrents.noaa.gov/stationhome.html?id=8447930 (visited on 05/13/2026).

[23] G. Ikeda. *Troubleshooting Basics: Profiling CTDs*. https://www.seabird.com/news/profiling-ctd-troubleshooting-basics. Sea-Bird Scientific. Accessed: 2026-04-26. Oct. 2018.

[24] National Ocean Service, NOAA. *Tidal Variations — The Influence of Position and Distance*. https://oceanservice.noaa.gov/education/tutorial_tides/tides06_variations.html. Tides and Water Levels Tutorial, National Oceanic and Atmospheric Administration. Accessed: 2026-04-26. 2024.

[25] Innovative Sensor Technology IST AG. *LFS1107 Conductivity Sensor Datasheet*. https://www.ist-ag.com/sites/default/files/downloads/DCLFS1107_E.pdf. Accessed: 2026-04-20.

[26] Texas Instruments. *TMP117AIDRVR: 0.1°C Digital Temperature Sensor, 48-bit EEPROM, PT100/PT1000 RTD Replacement*. https://www.ti.com/product/TMP117/part-details/TMP117AIDRVR. Accessed: 2026-04-20. 2026.

[27] KELLER Pressure. *Series 4LD*. https://us.keller-pressure.com/product?id=5e2f22709d8b1060a188c35e. Accessed: 2026-04-20. 2026.

[28] Atlas Scientific. *Mini Conductivity K 1.0 Kit (M-EC-KIT-1.0)*. https://atlas-scientific.com/kits/mini-conductivity-k-1-0-kit/. Accessed: 2026-04-20. 2026.

[29] Z. Zheng, Y. Fu, K. Liu, R. Xiao, X. Wang, and H. Shi. "Three-stage vertical distribution of seawater conductivity." *Scientific Reports*, **8**(1), 2018, p. 9916. DOI: 10.1038/s41598-018-27931-y. URL: https://www.nature.com/articles/s41598-018-27931-y.

[30] R. L. Gordon. *Acoustic Doppler Current Profiler: Principles of Operation — A Practical Primer*. Tech. rep. P/N 951-6069-00, 52 pp. San Diego, CA: RD Instruments, 1996.

[31] B. H. Brumley, R. G. Cabrera, K. L. Deines, and E. A. Terray. "Performance of a Broad-Band Acoustic Doppler Current Profiler." *IEEE Journal of Oceanic Engineering*, **16**(4), 1991, pp. 402–407. DOI: 10.1109/48.90905.

[32] Microchip Technology. *SA65 Chip Scale Atomic Clock (CSAC)*. https://www.microchip.com/en-us/products/clock-and-timing/components/atomic-clocks/embedded-atomic-oscillators/csac. Accessed: 2026-04-20. 2026.

[33] Teledyne Scientific & Imaging. *Teledyne Chip Scale Atomic Clock (TCSAC) Data Sheet*. https://www.teledyne-si.com/en-us/Products-and-Services_/Documents/Teledyne%20Chip%20Scale%20Atomic%20Clock/TCSAC%20Data%20Sheet%2010Mar2020.pdf. Document TSI-0839, Product Version P2. Accessed: 2026-04-20. Mar. 2020.

[34] D. L. Mills. *Network time protocol (NTP)*. Tech. rep. 1985.

[35] D. L. Mills. "A brief history of NTP time: Memoirs of an Internet timekeeper." *ACM SIGCOMM Computer Communication Review*, **33**(2), 2003, pp. 9–21.

[36] A. Vallat and D. Schneuwly. “Clock Synchronization in Telecommunications via PTP (IEEE 1588).” In: *2007 IEEE International Frequency Control Symposium Joint with the 21st European Frequency and Time Forum*. 2007, pp. 334–341. DOI: 10.1109/FREQ.2007.4319093.

[37] Seiko Epson Corporation. *TG-3541CE: 32.768 kHz DTCXO Datasheet*. https://www.mouser.com/datasheet/3/97/1/TG_3541CE_en.pdf. Accessed: 2026-04-20. 2020.

[38] BTech Acoustics. *BT-2RCL*. https://www.btechacoustics.com/products/bt-2rcl. Accessed: 2026-04-25. 2026.

[39] Blue Robotics Inc. *Watertight Enclosure Datasheet*. Rev. C.4, April 2026. Accessed: 2026-04-25. 2026.

[40] Blue Robotics Inc. *WetLink Penetrator*. https://bluerobotics.com/store/cables-connectors/penetrators/wlp-vp/. Compression gland penetrator for subsea electrical cables, 3.7–9.8 mm cable diameter, rated to 1000 m depth. SKU: WLP-VP. Accessed: 2026-04-25. 2026.

[41] S. Microelectronics. *STM32U535/U545*. https://www.st.com/en/microcontrollers-microprocessors/stm32u535-545.html. Accessed: 2026-05-08.

[42] Texas Instruments. *TPS22917x 1 V–5.5 V, 2-A, 80-mΩ Ultra-Low Leakage Load Switch*. Datasheet, Rev. B. Accessed: 2026-04-26. Dec. 2021. URL: https://www.ti.com/product/TPS22917.

[43] ScioSense B.V. *AS3933 LF Receiver IC*. https://www.sciosense.com/as3933-lf-receiver-ic/. Accessed: 2026-04-09. 2026.

[44] U.S. Geological Survey. *Specific Conductance*. Techniques and Methods Book 9, Chap. A6.3. Supersedes USGS Techniques of Water-Resources Investigations, book 9, chap. A6.3, version 1.2. U.S. Geological Survey, Feb. 2019, p. 15. DOI: 10.3133/tm9A6.3. URL: https://doi.org/10.3133/tm9A6.3.

[45] High Tech, Inc. *HTI-96-Min Hydrophone Series*. https://www.hightechincusa.com/products/hydrophones/hti96min.html. Accessed: 2026-05-12.

[46] E. Gallimore, J. Partan, I. Vaughn, S. Singh, J. Shusta, and L. Freitag. “The WHOI Micromodem-2: A Scalable System for Acoustic Communications and Networking.” In: Accessed: 2026-05-12. IEEE, 2010. URL: https://acomms.whoi.edu/wp-content/uploads/sites/20/2014/08/Micromodem2_2010.pdf.

[47] Raspberry Pi Ltd. *Raspberry Pi 5*. https://www.raspberrypi.com/products/raspberry-pi-5/. Accessed: 2026-05-12. 2023.

[48] HiFiBerry. *HiFiBerry DAC8x*. https://www.hifiberry.com/shop/boards/hifiberry-dac8x/. Accessed: 2026-05-12. 2024.

[49] HifiBerry. *HiFiBerry ADC8x add-on*. https://www.hifiberry.com/shop/boards/hifiberry-adc8x-add-on/. Accessed: 2026-05-12. 2024.

[50] Digi-Key Electronics. *ADXL366 Analog Devices Inc. | Motion Sensors*. https://www.digikey.com/en/products/base-product/analog-devices-inc/505/ADXL366/737925. Accessed: 2026-04-25.

[51] MEMSIC Semiconductor Co., Ltd. *MMC5603NJ AMR Magnetometer*. https://www.memsic.com/magnetometer-2. Accessed: 2026-04-25.